# Present day crustal vertical movement inferred from precise leveling data in eastern margin of Tibetan Plateau

Ming Hao [a], Qingliang Wang [a], Zhengkang Shen [b,c,*], Duxin Cui [a], Lingyun Ji [a], Yuhang Li [a], Shanlan Qin [a]

[a] Second Monitoring Center, China Earthquake Administration, Xi'an 710054, China
[b] Department of Earth, Planetary and Space Sciences, University of California, Los Angeles, CA 90095-1567, United States
[c] School of Earth and Space Science, Peking University, Beijing 100871, China

## ARTICLE INFO

## ABSTRACT

We collect precise leveling data observed in the period of 1970 to 2012 around the eastern margin of the Tibetan Plateau, and process the data to acquire present day crustal vertical velocity field. Vertical rates of 9 GPS sites are employed as a priori constraints to define the reference frame. The velocity field shows that most of the regions in the eastern margin of the Tibetan Plateau are undergoing uplift. The Gongga Shan and West Qinling are uplifting at maximum rates of $5.8 \pm 1.0$ mm/a and $6.0 \pm 1.3$ mm/a, respectively. A 2-D buried dislocation model is used to infer normal or reverse dip-slip rates. The result indicates that the reverse slip rate along the Longmen Shan fault is $4.2 \pm 0.5$ mm/a, followed by the Daliangshan and Longriba faults with the rates of $3.7 \pm 0.5$ mm/a and $2.8 \pm 0.3$ mm/a respectively. The Zemuhe and northern section of the Xiaojiang fault have the normal slip rates of $2.3 \pm 1.0$ mm/a and $2.9 \pm 0.4$ mm/a respectively. Combining vertical velocity field with GPS derived horizontal velocity field, we investigate the characteristics of crustal movement and dynamic mechanism. The 3D velocity field indicates that the Helan Shan is uplifting and the Yinchuan graben is subsiding. The 3D crustal movement of the Liupan Shan region is segmented, with the area in the vicinity of the northern Liupan Shan fault uplifting and the area in the vicinity of southern Liupan Shan fault subsiding respectively. The subsidence of the central and southern Sichuan–Yunnan terrain is caused by the near east–west extension. The budget of horizontal material influx suggests that movements of the upper and lower crust are rather different in most of the region, excessive material influx into the lower crust/upper mantle underneath most of the sub-blocks seems required to maintain the uplift rates inferred from leveling, providing evidence for the existence of lower crustal flow in this region.

## 1. Introduction

The collision between the Indian and Eurasian plates occurred in the early Cenozoic. Since then subduction of the Indian plate underneath the Eurasian plate has not only formed the Himalayan orogenic belt, but also created the Tibetan Plateau. Over the past four decades, a variety of geophysical dynamic models have been proposed to explain the uplift of the Tibetan Plateau. One school of thoughts suggests that the lateral extrusion of rigid or slowly deforming blocks via large strike-slip faults accommodates most of the India–Eurasia convergence (e.g. Peltzer and Tapponnier, 1988; Replumaz and Tapponnier, 2003; Tapponnier et al., 1982). Another school believes that the continents undergo distributed deformation, and the north–south shortening of the Tibetan Plateau is mostly accommodated by thickening of the Tibetan crust (e.g. England and McKenzie, 1982; England and Molnar, 1997; Houseman and England, 1986). Some interpret such distributed deformation by the existence of ductile lower crustal flow (e.g. Clark and Royden, 2000; Royden et al., 1997). Different models suggest conflicting crustal deformation patterns in the vicinity of the plateau, especially around its east margin (Shen et al., 2005). Thus, precise measurement of the three-dimensional crustal deformation in this region can provide important quantitative constraints to the dynamic models, and help understand the evolution and tectonics of the Tibetan Plateau.

During the past two decades, with the application of the Global Positioning System (GPS) technique to crustal deformation research, the horizontal velocity field in the eastern margin of the Tibetan Plateau has been obtained and continuously refined (Gan et al., 2007; Shen et al., 2001, 2005; Wang et al., 2001; Y.Z. Wang et al., 2008; Zhang et al., 2004). The GPS measurements can measure three-dimensional crustal deformation, but the accuracy of vertical positioning is much lower than that of the horizontal components, due to atmospheric refraction effect and uncertainties in the antenna phase centers of GPS satellites and receivers. Up to now most of the GPS observed deformation field utilized data from the Crustal Movement Observation

* Corresponding author at: Department of Earth, Planetary, and Space Sciences, UCLA, 3806 Geology, 595 Charles Yong Drive, Los Angeles, CA 90095-1567, United States. Tel./fax: +1 310 206 4070.
E-mail address: zhengkangshen@gmail.com (Z. Shen).

Network of China (CMONOC) project (Niu et al., 2002; M. Wang et al., 2003; Y.P. Wang et al., 2003). This network was first surveyed in 1998, and the GPS observations span for one and a half decades. By contrary, the precise leveling networks in this region have been measured since 1970s, and their measurements are capable of detecting vertical motion with accuracy of about one order of magnitude better than GPS (D'Anastasio et al., 2006). The precise leveling is therefore still a major technique used for obtaining the crustal vertical deformation, providing critical datasets for earthquake science research.

In this study, we use the available high-precision leveling data measured between 1970 and 2012, to infer the vertical velocity field in the eastern margin of the Tibetan Plateau. Combining with the GPS horizontal velocity result of previous studies, we analyze the characteristics of the three-dimensional crustal movement of the eastern margin of the Tibetan Plateau, and discuss the geodynamic mechanisms of crustal deformation constrained using the 3D deformation dataset.
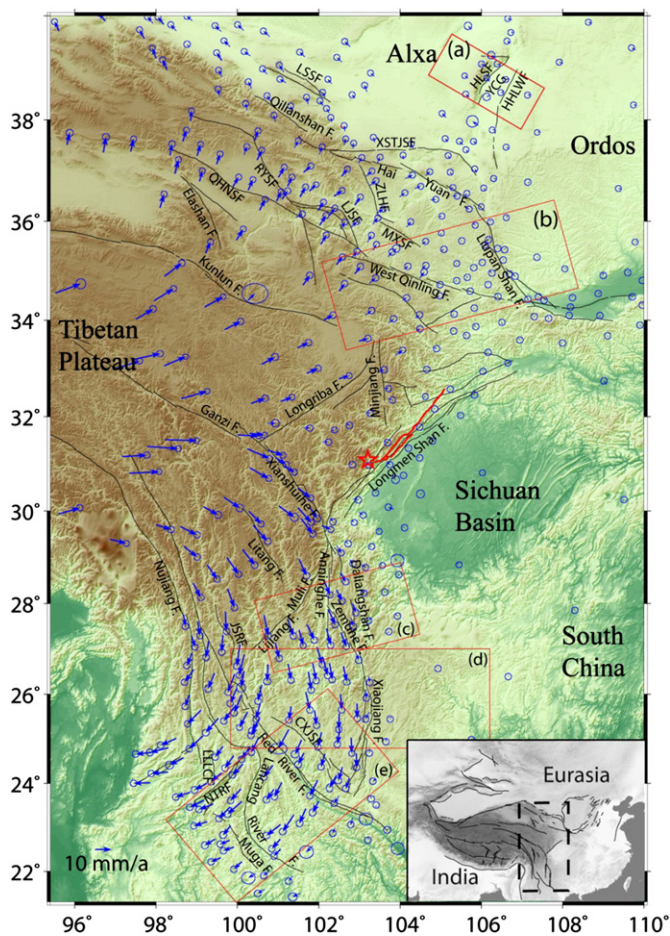


**Fig. 1.** GPS horizontal velocity field for the eastern margin of the Tibetan Plateau (with respect to the South China block). The study area is depicted in the inset map. The error ellipses represent 70% confidence. The red rectangles delineate GPS sites included in GPS velocity profile diagrams across a selected group of active faults. The red star is the epicenter of 2008 Wenchuan earthquake, China, and the red solid curves are the surface rupture caused by this earthquake. The black solid lines indicate active faults in Holocene (Deng et al., 2003). Abbreviations are: HLSF, Helan Shan fault; HHLWF, Huanghe–Lingwu fault; YCG, Yinchuan graben; LSSF, Longshoushan fault; XSTJSF, Xiangshan–Tianjingshan fault; ZLHF, Zuanglanghe fault; MXSF, Maxianshan fault; RYSF, Riyueshan fault; LJSF, Lajishan fault; CXJF, Chuxiong–Jianshui fault; JSRF, Jinsha River fault; LLLF, Longling–Lancang fault; NTHF, Nanting River fault.

## 2. Tectonic setting and horizontal velocity field

The eastern borderland of the Tibetan Plateau is tectonically active. The northern part of the eastern margin of the Tibetan Plateau undergoes active orogenic and faulting processes around the western Qinling and Longmen Shan Mountains. Its southern part is composed of a network of active faults, from the left-lateral Xianshuihe–Anninghe–Xijiang fault in the north and east, and the right-lateral Nujiang, Lijiang–Xiaojinhe, and Red River fault systems in the west and south (Ma et al., 1989). The eastern margin of the Tibetan Plateau separates stable blocks of Ordos, Sichuan basin, and South China to the east from the strong uplift of the Tibetan Plateau to the west (Fig. 1). Geophysical structural exploration studies show that the Tibetan Plateau crust is about 60–70 km thick, while the crustal thickness of North and South China is only about 40–50 km (Ding, 1991). The eastern margin of the Tibetan Plateau also has a strong gravity gradient and sharp crustal thickness change across. Late Cenozoic and present day tectonic deformation patterns on both sides of the eastern margin of the Tibetan Plateau are markedly different. Large-scale active faults are located to the west of and along the boundary of the plateau and are often struck by strong earthquakes, while to the east of the boundary faulting and earthquake activities are much less. On May 12, 2008, a devastating Ms8.0 earthquake occurred in the Longmen Shan region along the Longmen Shan fault, which is located at the central part of the eastern margin of the Tibetan Plateau. This earthquake is the most recent devastating seismic event attesting the ongoing tectonic activity in the eastern margin of the Tibetan Plateau.

In this study we combine vertical leveling data and horizontal GPS velocities to study 3D deformation field in the region. GPS data are mainly from the CMONOC project observed in the period of 1998–2007. The GPS horizontal velocity solution is from Wang (2009). In order to show the interior deformation of China, the velocity field is transformed from the ITRF2005 reference frame to a regional reference frame with respect to the South China block (Fig. 1). We first compute a common angular velocity pole of the South China block relative to the ITRF2005 reference frame. We then eliminate potential outliers from the GPS station velocities through an iteration procedure, each time removing a site with the largest postfit residual and redo the angular velocity estimation, until all the postfit residual velocities are within 2 mm/yr. Finally the GPS velocity field is converted to the south China reference frame by using the estimated angular velocity (Wang, 2009).

## 3. Leveling data

The precise leveling data observed around the eastern margin of the Tibetan Plateau were collected from two leveling networks. The first one is part of the Leveling Networks Used for Seismic Applications (LNUSA) spanning the major active faults in China and surveyed by the China Earthquake Administration (CEA) for the period of 1970 to 2009, and the second one is part of the national leveling networks of China observed by the National Administration of Surveying, Mapping and Geoinformation (NASMG) during 1977–1988, 1991–1999, and 1982–1988, respectively. All the LNUSA networks were surveyed in the first-order leveling. The national leveling networks were surveyed in the first-order leveling during 1977–1988 and 1991–1999, and in the second-order leveling during 1982–1988. As part of the project of "Integrated Geophysical Field Observation — the eastern margin of the Tibetan Plateau", the national leveling networks in the central and western Yunnan region were also resurveyed between 2010 and 2012 in the first-order leveling by CEA. The amount of second-order observations accounts for 2.5% of overall observations. The leveling routes and their surveying time spans are shown in Fig. 2. As a quality check, the misclosures computed from forward and backward leveling of LNUSA are within ±0.4 mm/km. The misclosures are within ±0.5 mm/km
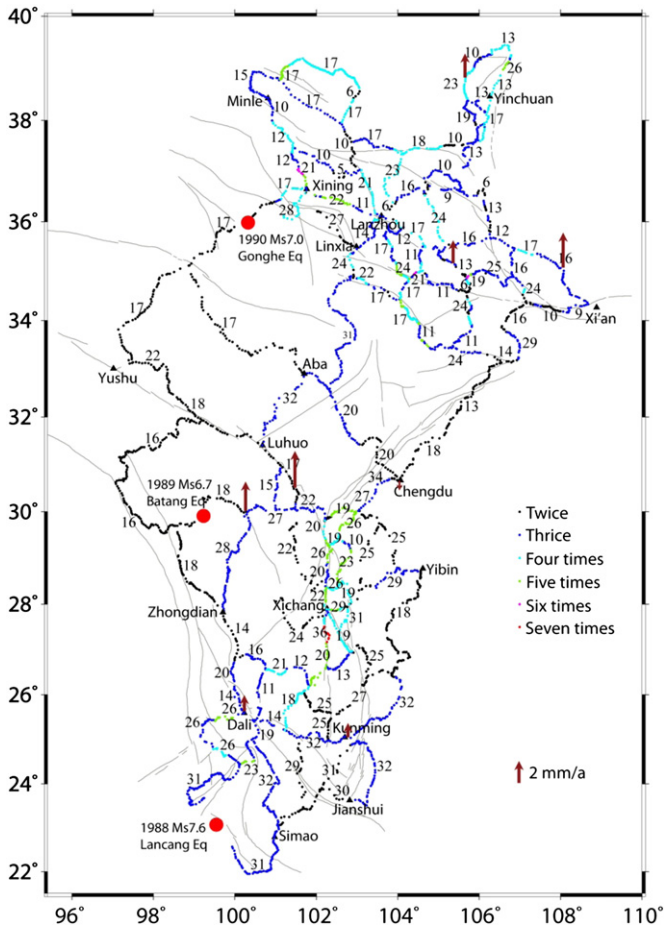
**Fig. 2.** Map showing leveling routes and their surveying time spans. The dots show the locations of the leveling benchmarks, whose colors denote the number of survey epochs. The numbers next to the routes indicate the duration years between the first and last observations. The red solid circles denote the three earthquakes which contaminated the leveling measurements. The dark brown vectors are the vertical velocities of nine GPS stations listed in Table 1.

and ± 1.0 mm/km for the first-order and second-order leveling of the national leveling network, respectively (Lai et al., 2004).

## 4. Methods

### 4.1. Benchmark instability checking

Detection and removal of unstable benchmarks from the leveling datasets are important for quality control of the data. In order to check the unstable benchmarks caused by sediment compaction, ground water withdrawing or destruction due to human activities, all the height differences between the adjacent benchmark pairs are plotted over time. The benchmarks with anomalous elevation changes with respect to the neighborhood sites are therefore identified and removed, and their leveling observations with respect to their two neighboring benchmarks are combined and treated as the observations between these two neighborhood benchmarks. For all the earthquakes of Ms ≥ 6 that occurred between January 1970 and May 2012 (catalog is from the China Earthquake Networks Center), three events affected the height differences. The three earthquakes are the Ms7.6 Lancang–Gengma occurred November 6, 1988 in Yunnan Province, Ms6.7 Batang occurred April 16, 1989 in Sichuan Province, and Ms7.0 Gonghe occurred April 26, 1990 in Qinghai Province, respectively. The height differences between the adjacent benchmarks contaminated by the coseismic deformation are also detected in the time series of elevation changes, and

the contaminated height differences are integrated and used as a substitute measurement between the two neighborhood benchmarks.

### 4.2. A priori uncertainty estimation

We choose the network in the Yunnan region to estimate and test the a priori uncertainty. The total length of the network routes is 4000 km. This region is selected for the test because only in this region were repeated surveys conducted in 2010 and 2011, and no noticeable vertical movements for benchmarks within this short time period are found. Hence, the correction for the height difference can be estimated using the classic least-square adjustment and the uncertainty of height difference per unit distance can be obtained. The result shows that the standard deviation of height difference is 1.2 mm/km, which is consistent to the standard error of the first order of leveling survey (1 mm/km) required by the Specifications for the First and Second Order Leveling of China (SFSOLC, Standardization Administration of the People's Republic of China, 2006).

### 4.3. Linear dynamic adjustment

In this study we assume a constant vertical displacement rate of the field in the region, and perform linear dynamic adjustment of the leveling data using the least-square method. This assumption is an approximation of the secular vertical deformation field averaged over several decades, and its validity will be assessed in the following section. Let the vertical rate of the $i$-th benchmark be denoted as $V_i$, and the elevation of the benchmark $H_i^t$ at time $t$ be:

$$H_i^t = H_i^0 + V_i(t - t_0) \tag{1}$$

where $t_0$ is the reference time, and $H_i^0$ is the elevation at the reference time. The height difference between benchmarks $i$ and $j$ is then:

$$\begin{aligned} h_{ij}^t &= H_j^t - H_i^t \\ &= H_j^0 + V_j(t - t_0) - H_i^0 - V_i(t - t_0) \\ &= \left(H_j^0 - H_i^0\right) + \left(V_j - V_i\right)(t - t_0) \end{aligned} \tag{2}$$

where $H_j^0$, $H_i^0$, $V_j$, and $V_i$ are the elevation and velocity parameters for the $i$-th and $j$-th benchmarks respectively. The velocity estimation can be obtained by the least-square method:

$$\varepsilon = \mathbf{AX} - (\mathbf{L} - \mathbf{AX_0}) \tag{3}$$

where $\mathbf{L}$ is the observation array composed of height difference $h_{ij}^t$, $\mathbf{A}$ is the design matrix, $\mathbf{X}$ is the array of adjustment for unknown parameters, $\mathbf{X_0}$ is the array of approximate values for unknown parameters, $\varepsilon$ is the array of adjustment for observation of height difference $h_{ij}^t$. The unknown parameters contain the vertical rates of all the benchmarks and corresponding elevations at time $t_0$. The weight matrix of observations is $\mathbf{P}$. The weight for observation between benchmarks $i$ and $j$ is

$$P_{ij} = 1 / \left(\sigma_w^2 L_{ij}\right) \tag{4}$$

where $L_{ij}$ is the distance between benchmarks $i$ and $j$, and $\sigma_w$ is the standard error of corresponding order of leveling survey. According to SFSOLC, the standard errors for the first and second orders of leveling survey are 1 mm/km and 2 mm/km respectively.

### 4.4. Linear rate assumption testing

For the linear model, having determined the benchmark vertical rate $V_i$ and the initial elevation height, we can calculate the model prediction $V_i(t - t_0)$, the observation $H_i^t - H_i^0$, and the residual between them at
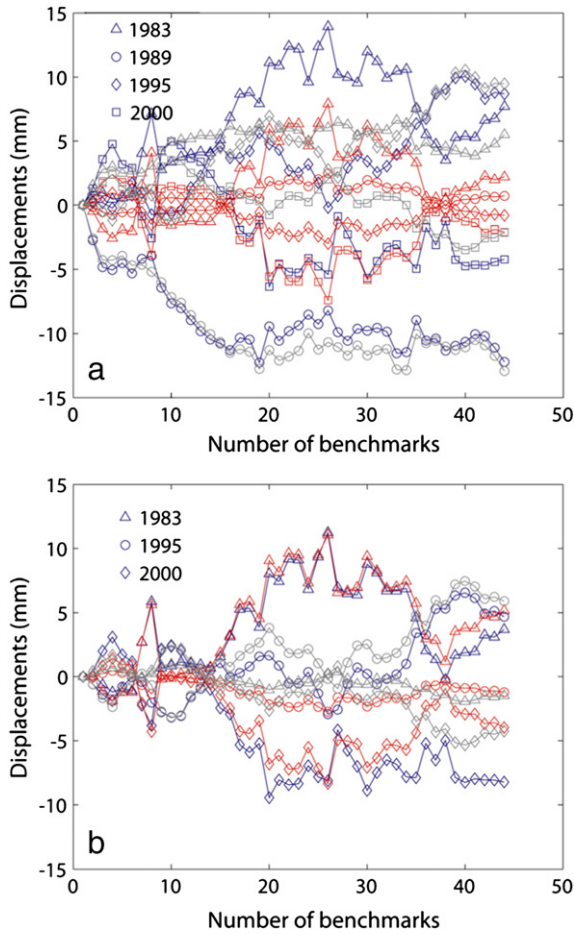
Fig. 3. An example of linear displacement model fitting. The blue lines are the observations $H_i^t - H_i^0$, the red lines are the model predictions $V_i(t - t_0)$, and the gray lines are the model postfit residuals. (a) Leveling data along routes with the anomalous epoch of 1989 included. (b) Leveling data along routes with the epoch of 1989 removed.

each observation time epoch $t$. The postfit residual $\chi^2$ for all the data of each route can also be obtained. If one leveling route was resurveyed more than three times, a ratio $C$ can be given as follows,

$$C(k) = \chi_k^2 \Big/ \sum_{j=1}^{n} \frac{\chi_j^2}{n} \qquad (5)$$

where $j$ is the number of observation epochs ($j = 1,...,n$). If the ratio $C(k)$ is greater than a given threshold, the observations of this leveling route at the $k$-th epoch are considered as abnormal and removed. After some trial cases we set the abnormal threshold at 2.0.

Fig. 3 shows such an example. The leveling surveys were conducted in 1983, 1989, 1995 and 2000. The posterior residuals $\chi^2$ for the four epochs are 1102.9, 4420.4, 1374.3 and 147.5, and the corresponding $\chi^2$ ratios are 0.6, 2.5, 0.8 and 0.1 respectively (Fig. 3(a)). The observations in the 1989 epoch seem to be outliers, and therefore are filtered out. The filtered posterior residuals $\chi^2$ for the remaining three epochs are 32.1, 495.9 and 255.9, and the values of $C(k)$ are 0.1, 1.9 and 1.0 respectively (Fig. 3(b)).

In this study we have collected data from leveling routes of ~26,000 km in total length, among which ~4200 km have been surveyed more than three times during the four decades of time span. We perform the above error analysis for all the leveling data of these 4200 km, and find that the data of 2300 km are contaminated by outliers

(with the corresponding C > 2.0). The data of anomalous epochs are removed.

### 4.5. Systematic error mitigation

The height differences between the adjacent pairs of benchmarks are affected by systematic and random errors, the former being the main source of errors. Most systematic errors can be reduced or mitigated by following the procedure of SFSOLC, but a few systematic errors such as the rod calibration errors may still exist.

In order to discriminate the systematic errors accumulated over long distance, we use the vertical rates of nine GPS stations (Wang, 2009) located within the studied region as the a priori constraints. GPS data are from the CMONOC project observed from 1998 to 2008. Four GPS sites are continuous stations and five are annually observed campaign stations with an occupation of ~7 days each year. These GPS sites are not tied directly to the leveling benchmarks, but the distances between these GPS stations and local leveling benchmarks are all within a few kilometers, and the GPS stations and the nearest leveling benchmark are all far away from active faults (Fig. 2). We therefore assume that each leveling benchmark shares a common vertical displacement rate with its nearby GPS site. The vertical rates of nine GPS stations are listed in Table 1.

### 4.6. GPS a priori constraints

The leveling surveys are relative measurements, to obtain absolute elevations and velocities both references for elevation and velocity must be given. Conventional leveling geodesy usually chooses the elevation and velocity of a benchmark or some quasi-stable benchmarks as reference. But in this study, we choose the vertical velocity of GPS stations mentioned in Section 4.5 as the velocity reference, and the elevation of a benchmark located in the Sichuan Basin as zero reference.

Let the vertical rates of the 9 GPS sites (Table 1) and the benchmarks closest to the 9 sites be denoted as $v_i^{GPS}$ and $v_i^{lev}$ respectively, the a priori constraints for the vertical velocities of these benchmarks are then given as:

$$v_i^{lev} = v_i^{GPS} \qquad (6)$$

and adjustments of these velocities are loosely constrained to zero with finite uncertainties defined by GPS data. The constraining equations are then given as:

$$\mathbf{GX} + \mathbf{s} = \mathbf{0} \qquad (7)$$

$\mathbf{G}$ is a simple matrix composed of 0 and 1, $\mathbf{X}$ is the vector of adjustments of these 9 benchmarks' velocities from a priori, and $\mathbf{s}$ is the vector of errors of the GPS vertical velocities listed in Table 1 and the errors of elevations for reference benchmarks. Actually, the elevations of benchmarks are not the focus of our study, so the error of the reference

**Table 1**
GPS vertical velocity.

| Site | Coordinate | | Distance[a] (km) | Vertical velocity (mm/a) |
|------|------------|--|----------|---------------|
| | Longitude (°) | Latitude (°) | | |
| CHDU | 104.06 | 30.64 | 3.7 | −0.9 ± 1.8 |
| XIAG | 100.26 | 25.61 | 2.3 | 1.5 ± 1.4 |
| KUNM | 102.80 | 25.03 | 4.8 | 1.3 ± 1.7 |
| XNIN | 101.77 | 36.60 | 2.3 | −0.3 ± 0.4 |
| JB08 | 108.09 | 35.06 | 5.1 | 3.2 ± 1.3 |
| JB09 | 105.67 | 38.81 | 1.0 | 2.2 ± 1.3 |
| JB27 | 105.38 | 35.14 | 2.2 | 2.1 ± 1.2 |
| JB35 | 101.50 | 30.50 | 3.2 | 3.3 ± 2.1 |
| JB40 | 100.28 | 29.99 | 0.4 | 2.7 ± 1.5 |

[a] Distance between the GPS site and the closest benchmark.

benchmark elevation can be set to a small number (such as 0.1 mm). Using the observation Eq. (3), constraint Eq. (7) and the least-square regression, the solution is given as

$$\mathbf{X} = \left(\mathbf{A}^T \mathbf{P} \mathbf{A} + \mathbf{G}^T \mathbf{P}_w \mathbf{G}\right)^{-1} \mathbf{A}^T \mathbf{P} \mathbf{L}$$
$$\sum{}_{\mathbf{X}} = \left(\mathbf{A}^T \mathbf{P} \mathbf{A} + \mathbf{G}^T \mathbf{P}_w \mathbf{G}\right)^{-1} \hat{\sigma}_0^2 \tag{8}$$

where $\mathbf{P}_w$ is the weight matrix of a priori constraints. The diagonal elements of $\mathbf{P}_w$ are the reciprocals of the squares of uncertainties of GPS vertical velocities. $\hat{\sigma}_0$ is the a posteriori uncertainty,

$$\hat{\sigma}_0^2 = \mathbf{V}^T \mathbf{P} \mathbf{V}/(m + d + 1 - 2n) \tag{9}$$

where $m$ is the number of observations, $n$ the number of benchmarks, and $d$ the number of a priori GPS vertical velocities.

According to inverse theory, the resolution of a solution can be expressed as (Jackson and Matsu'ura, 1985):

$$\mathbf{R} = \left(\mathbf{A}^T \mathbf{P} \mathbf{A} + \mathbf{G}^T \mathbf{P_w} \mathbf{G}\right)^{-1} \mathbf{A}^T \mathbf{P} \mathbf{A}. \tag{10}$$

GPS and leveling are different observation techniques and have completely different error sources. It is needed to assign an appropriate relative weighting between the two datasets. Let the weight ratio between $\mathbf{P}$ and $\mathbf{P}\mathbf{w}$ in Eq. (8) be denoted as $k$, and we elect to determine $k$ through examining the trade-off between the resolution of solution and leveling data postfit residual $\chi^2$ (Fig. 4). From the curve we can see that as $k$ decreases resolution increases and the postfit residual $\chi^2$ decreases, but the solution becomes less stable.

In Fig. 4, the vertical line AB denotes the resolution when the solution is constrained completely, while the horizontal line AC means the minimum postfit residual $\chi^2$ when the solution is free of constraint. The line OB is the asymptote extrapolated from three of the largest postfit residual $\chi^2$ points, and the line OC is the asymptote extrapolated from three of the least postfit residual $\chi^2$ points. The cross point connecting line OA and the trade-off curve denotes the optimal constraint for the inversion, where point O is the cross point of the two asymptote lines, and point A is the cross point of the least residual and least resolution of the model (Wan et al., 2008). An optimal solution is the one on the curve which is "farthest" from the two extremes and the associated linear trends, and this method provides a way to locate the right solution on the curve. In this case we determine the optimal $k$ as of 0.3.
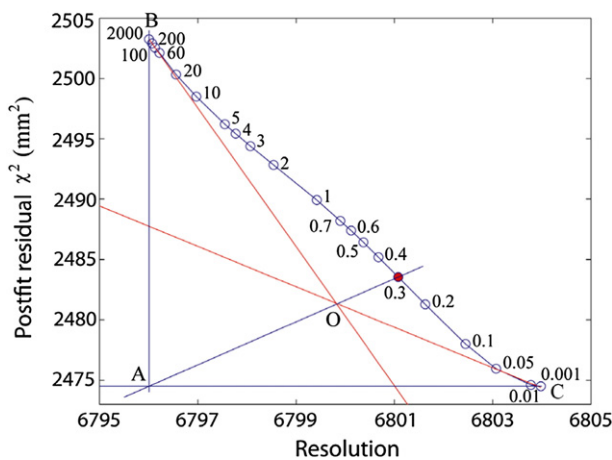


**Fig. 4.** The trade-off curve between resolution and postfit residual $\chi^2$. The numbers are the weight ratios between GPS and leveling measurements.
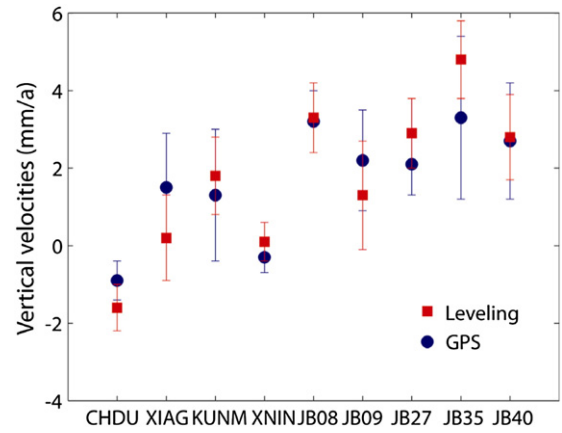


**Fig. 5.** Vertical velocities obtained by GPS stations and the closest leveling benchmarks. Error bars denote $1\sigma$.

Fig. 5 shows the difference of vertical velocities between GPS and leveling data at nearby benchmarks. We can see that the maximum discrepancy is 1.5 mm/a, while the minimum is 0.1 mm/a.

## 5. Results

After the least-square adjustment, the estimation of posterior variance $\hat{\sigma}_0^2$ which can be derived from Eq. (9) equals 1.0 mm$^2$/km$^2$, which is statistically consistent with the a priori variance at 95% confidence level, thus the adjustment model is reasonable.
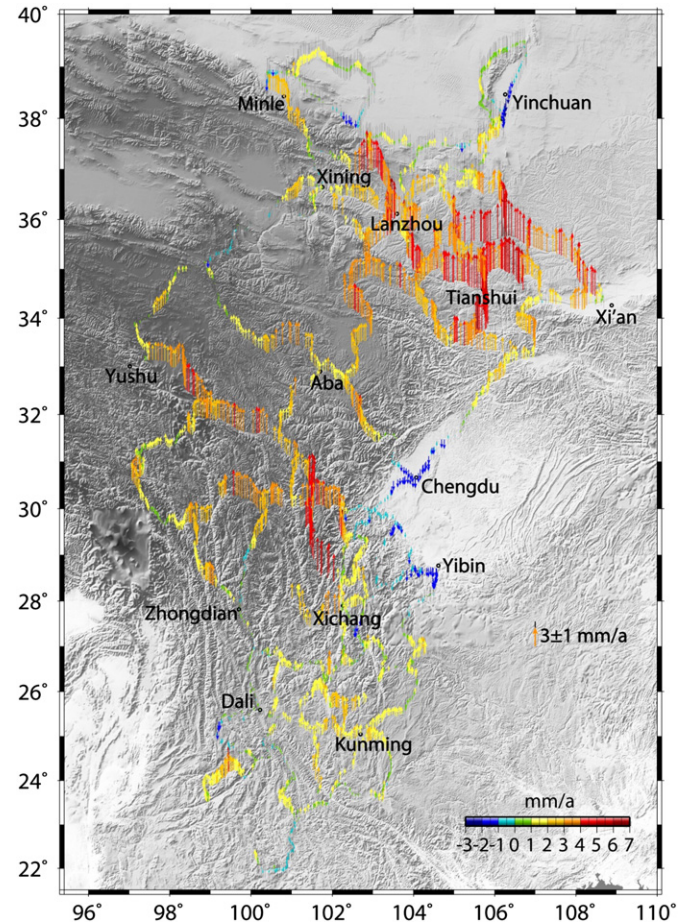


**Fig. 6.** Leveling derived vertical velocity field across the eastern margin of the Tibetan Plateau.

The trend of long-term crustal vertical movement obtained in this paper is consistent with existing results inferred from geological methods (Hubbard and Shaw, 2009; Kirby et al., 2002, 2003; Lease et al., 2011; Tan et al., 2010), GPS (Freymueller et al., 2010; Liang et al., 2013; Wang, 2009), and leveling measurements (Ma et al., 2003; Q.L. Wang et al., 2008). Most regions of the eastern margin of the Tibetan Plateau are in the status of uplift (Fig. 6), especially the Gongga Shan uplifts at a maximum rate of 5.8 ± 1.0 mm/a, and the West Qinling Mountain goes up at a rate of 6.0 ± 1.3 mm/a. In the following sections we combine the vertical and horizontal velocity fields to analyze three-dimensional crustal movement across the major active faults and regions in eastern margin of the Tibetan Plateau.

### 5.1. Helan Shan–Yinchuan region

Helan Shan–Yinchuan region is an intraplate deformation belt in the western margin of North China Craton (region (a) in Fig. 1). This region is surrounded by stable blocks with the Alxa block to the west and the Ordos block to the east. To the southwest, numerous active strike-slip and thrust faults constitute the northeastern margin of the Tibetan Plateau. The GPS horizontal velocity profile can be used to acquire the relative motion rate across the fault. Fig. 7 shows right lateral motion of 1.7 ± 0.8 mm/a and extension of 0.9 ± 0.8 mm/a across the Helan Shan fault. The vertical velocity profile (Fig. 8) shows that the Yinchuan graben is in subsidence relative to the Helan Shan located west of the Helan Shan fault, which is consistent with the extension of the basin indicated by GPS. The center of subsidence or a large sinking area in the Yinchuan graben coincides with geologically determined subsidence center in the Quaternary (Chai et al., 2011), suggesting that the tectonic extensional deformation formed in early Paleogene is still ongoing today.

### 5.2. Liupan Shan region

The N15°W trending Liupan Shan, where folding and thrust faulting take place, forms the northeasternmost edge of the plateau (Zhang et al., 2004). The GPS profile perpendicular to the Liupan Shan indicates 6.0 ± 2.0 mm/a shortening parallel N75°E, and the wide distribution of strain suggests that shortening is not localized at the Liupan Shan, but spanning a range of about 300 km west of Liupan Shan (Fig. 9) (Zhang et al., 2004).

The vertical movements for the northern section (north of Jingyuan, Figs. 9 and 10) and the southern section (south of Jingyuan, Figs. 9 and 11) of the Liupan Shan are different. The region with the maximum
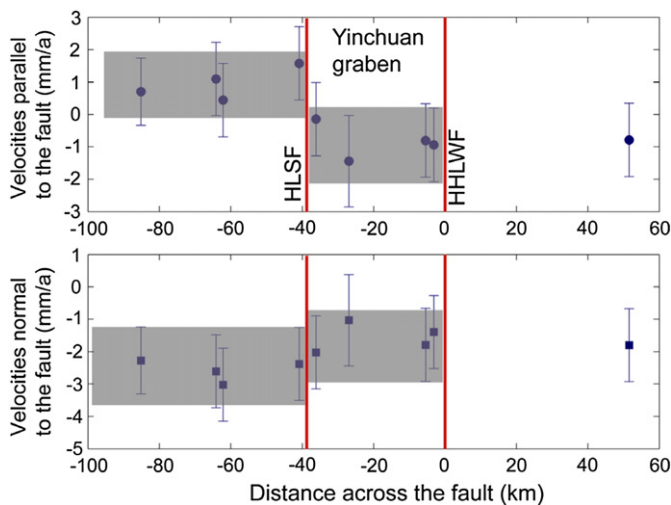


**Fig. 8.** Leveling vertical velocity profile across Helan Shan fault. The velocities are plotted as a function of distance normal to the fault. The red triangles in the inset map are the locations of the leveling benchmarks. Abbreviations are: HLSF, the Helan Shan fault; HHLWF, the Huanghe–Lingwu fault.

uplift rate is near the Liupan Shan fault in the northern section, while the largest uplift rate of the southern section is 20 km west of the fault. As shown in the GPS velocity field (Fig. 9), there is significant crustal shortening across the northern section, while there is no shortening or even east–west extension across the southern section. All these results suggest that the three-dimensional crustal movement of the Liupan Shan region has obvious segmentation characteristics.

### 5.3. Longmen Shan–Longriba region

The Longmen Shan rises ~4 km above the Sichuan basin and exhibits greater relief than anywhere else on the plateau (Hubbard and Shaw, 2009). The GPS velocities (Chen et al., 2000; Shen et al., 2005; Zhang et al., 2004) indicate ~3 mm/a convergence across the Longmen Shan orogenic and fault system. The Longriba fault, located ~200 km northwest of and parallel to the Longmen Shan, slips at a rate of 5.4 ± 2.0 mm/a right laterally and converges at a rate of 0.55 mm/a (Shen et al., 2005; Xu et al., 2008).



**Fig. 7.** GPS horizontal velocity profiles across Yinchuan graben. The data are from the rectangle (a) region in Fig. 1. Upper panel: Fault-parallel component; lower panel: fault-normal component. Gray bars depict the scattering range of data on both sides of a fault. Abbreviations are: HLSF, the Helan Shan fault; HHLWF, the Huanghe–Lingwu fault.
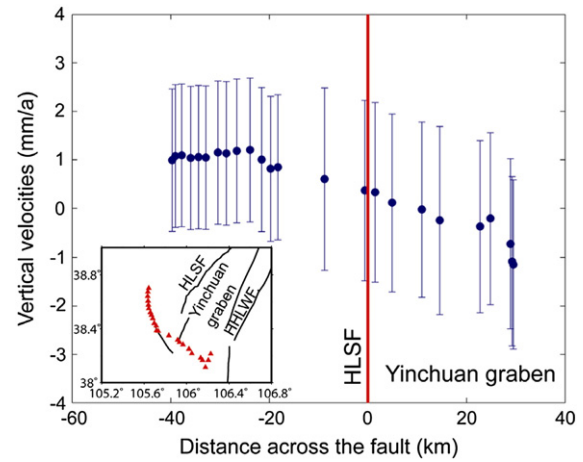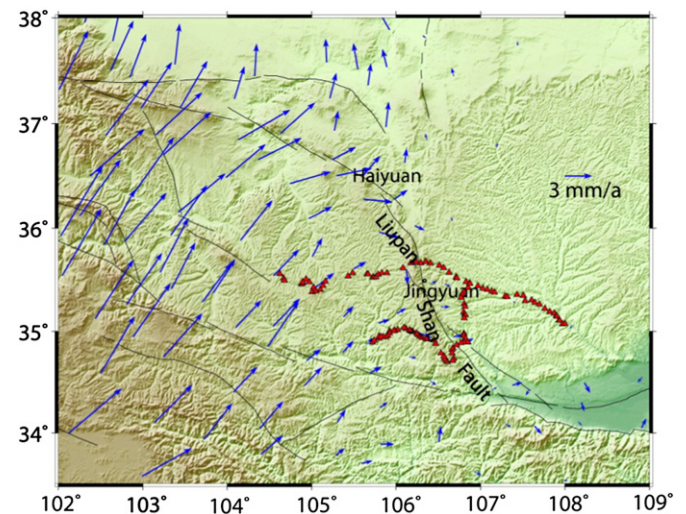


**Fig. 9.** GPS velocity field for the northeastern margin of the Tibetan Plateau with respect to the Ordos block. The data are from the rectangle (b) region in Fig. 1. The red triangles are the two leveling routes (Figs. 9 and 10) across the Liupan Shan fault.
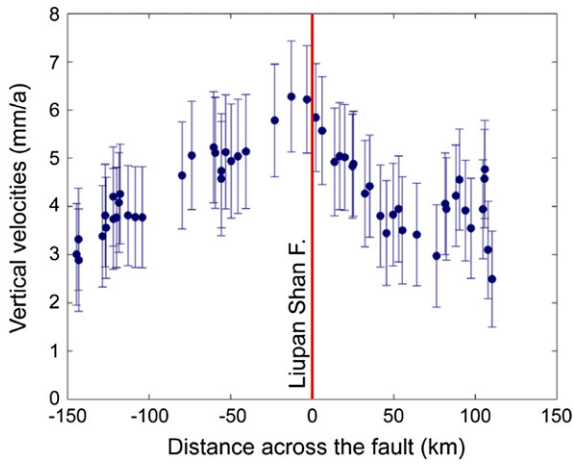
Fig. 10. Vertical velocity profile across northern segment of Liupan Shan fault. The leveling route is nearly normal to the fault.

In order to obtain the interseismic reverse dip-slip rate along the Longmen Shan and Longriba faults, we use the Okada dislocation model (Okada, 1985) to simulate fault slip across the two faults (Fig. 12). The surface location of the fault was acquired from Deng et al. (2003). The Longmen Shan fault is composed of the Maowen, Beichuan, and Pengguan faults and dips NW (Shen et al., 2009). The Longriba fault consists of the Longriqu and Maoergai faults and dips NW (Xu et al., 2008). These fault systems are part of a ramp system in the upper crust, connecting to a horizontal detachment in mid-crust at the depth of 30 km (Xu et al., 2008). In our model these fault patches are rectangular in size and expanded on both sides to 1000 km, and the locking depths of the two fault systems are assumed to be the same. The dip-slip rate of each fault zone is the sum of dip-slip rates of its sub-faults. Since the dip angle may not be sensitive to leveling data, it can be fixed at 45°. The locking depth is a nonlinear parameter to the data, so the grid search method is used to obtain the optimal solution, determined by weighing on the postfit residual $\chi^2$. The dip-slip rates were estimated by least-square adjustment.

Our solution shows that the reverse dip-slip rates along the Longmen Shan and Longriba fault systems are 4.2 ± 0.5 and 2.8 ± 0.3 mm/a respectively with the locking depth of 22 km, and the dip-slip rate along the detachment is 4.3 ± 0.8 mm/a. The dip-slip rate along the Longriba fault obtained from the leveling is slightly larger than the result of 0.7 mm/a of Xu et al. (2008) inferred from satellite
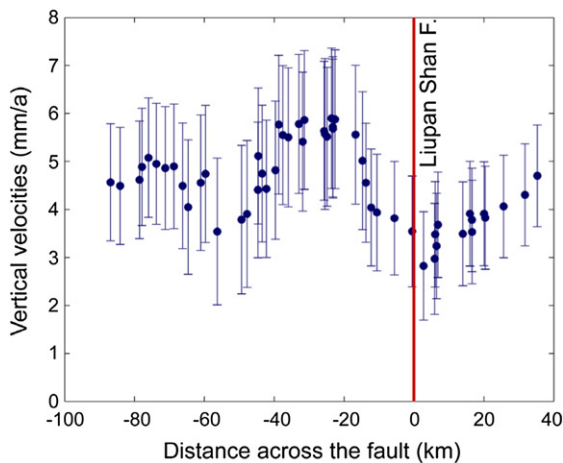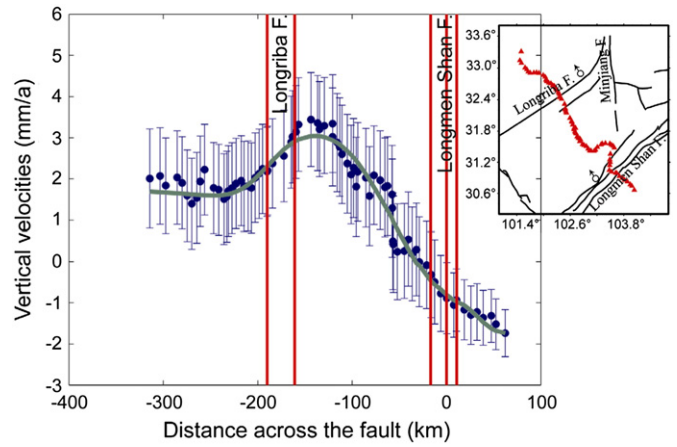


Fig. 12. Vertical velocity profile across the Longmen Shan–Longriba region. The velocities are plotted as a function of distance normal to the fault. The green curve is the modeling result across the two faults. The Longriba fault is composed of the Longriqu and Maoergai faults, and the Longmen Shan fault consists of the Maowen, Beichuan, and Pengguan faults. The red triangles in the inset map are the locations of the leveling benchmarks. The dipping directions of the Longriba and Longmen Shan faults are denoted by the symbol of "♂".

image interpretation and field investigation. Forward predictions of horizontal displacements from our model agree approximately with the GPS velocities, although precise comparison between the two requires a 3-D instead of 2-D deformation model.

### 5.4. Sichuan–Yunnan block

The Sichuan–Yunnan block is defined as a fragment of crust southeast of Tibet being extruded out of the plateau. It is delineated by the Xianshuihe–Xiaojiang fault system to the north and east, and the Nujiang and Red River fault systems to the west and south, respectively (Fig. 1). Most of the regional deformation is around the block boundaries, and we focus on a few profiles across the boundary segments.

The GPS velocity profile parallel to the Zemuhe and Daliangshan faults (data from area (c) in Fig. 1) shows 4.1 ± 0.8 and 5.2 ± 0.8 mm/a left motion across the faults respectively (Fig. 13). There is no significant fault-normal deformation across the Zemuhe and Daliangshan faults (Fig. 13). Deformation modeling of the vertical motion profile across



Fig. 11. Vertical velocity profile across southern segment of Liupan Shan fault. The leveling route is nearly normal to the fault.
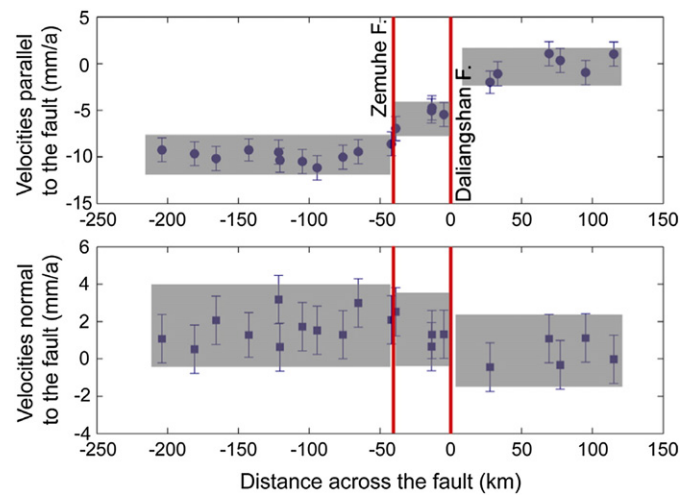


Fig. 13. Horizontal velocity profiles across Zemuhe and Daliangshan faults. The data are from the rectangle (c) region in Fig. 1. (Up) Fault parallel and (bottom) fault-normal components.
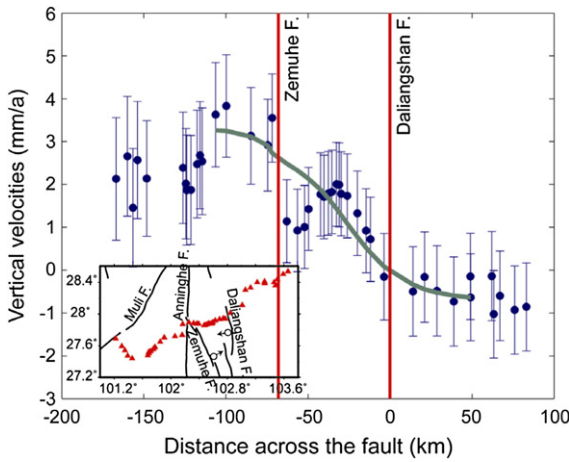
**Fig. 14.** Vertical velocity profile across Zemuhe and Daliangshan faults. The velocities are plotted as a function of distance normal to the fault. The green curve is the modeling result across the two faults. The red triangles in the inset map are the locations of the leveling benchmarks. The dipping directions of the Zemuhe and Daliangshan faults are denoted by the symbol of "♂".



**Fig. 16.** Vertical velocity profile across Xiaojiang fault. The velocities are plotted as a function of distance normal to the fault. The green curve is the modeling result. The red triangles in the inset map are the locations of the leveling benchmarks. The dipping direction of the Xiaojiang fault is denoted by the symbol of "♂".

the Zemuhe and Daliangshan faults, which dip NE and SW with the assumption of fixed 45° dipping, indicates that the normal and thrust dip-slip rates are 2.3 ± 1.0 and 3.7 ± 0.5 mm/a with the locking depths of 18 and 15 km, respectively (Fig. 14). Therefore, the extensional and convergent rates of 1.6 and 2.6 mm/a can be acquired from the dip-slip rates across the Zemuhe and Daliangshan faults. The overall ~1 mm/a horizontal convergence across the two fault systems derived from leveling is consistent with the GPS result (Fig. 13). Using the earthquake catalog data, Han and Jiang (2005) found that more moderate and strong earthquakes occurred along the Anninghe–Zemuhe fault than along the Daliangshan fault in the past 100 years. Y.Z. Wang et al. (2008) believed that across the Anninghe–Zemuhe fault, the average fault slip rate is larger and the average recurrence time interval of strong earthquakes is shorter than that across the Daliangshan fault, suggesting more release of seismic strains along the Anninghe–Zemuhe fault during the past centuries. Nevertheless, the three-dimensional motions suggest that the slip rate across the Anninghe–Zemuhe fault is less than that across the Daliangshan fault. We therefore infer that significant amount of elastic strains might have been accumulating
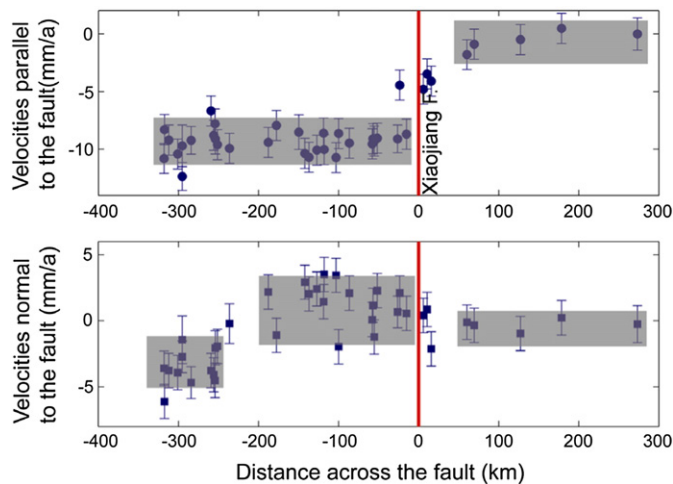
more along the Daliangshan fault than along the Anninghe–Zemuhe fault, with more increased seismic risk along the former than the latter.

We determine from GPS data a left-lateral motion rate of 8.8 ± 0.7 mm/a and little fault normal motion across the northern section of the Xiaojiang fault (Fig. 15). Our result is consistent with Zhang et al. (2003) and Shen et al. (2005). To the west of the Xiaojiang fault, deformation of the Sichuan–Yunnan block exhibits east–west extension inferred from a GPS profile perpendicular to the fault (Fig. 15). The normal slip rate along the northern section of the Xiaojiang fault is 2.9 ± 0.4 mm/a inferred from leveling data modeling, with a locking depth of 20 km and dipping of NE (Fig. 16). Such a fault motion model would predict about 2.0 mm/a horizontal extension across the fault, consistent with the GPS observation (Fig. 15).

Fig. 17 shows the horizontal movement across the southeast section of the Red River fault and the adjacent faults. About 1.6 ± 0.6 mm/a right motion and 1.2 ± 0.6 mm/a extension across this section of the Red River fault are found. The deformation rates are consistent with the results reported by Weldon et al. (1994), Duong and Feigl (1999), Guo et al. (2001), Feigl et al. (2003) and Shen et al. (2005). The



**Fig. 15.** Horizontal velocity profiles across Xiaojiang fault. The data are from the rectangle (d) region in Fig. 1. (Up) Fault parallel and (bottom) fault-normal components.
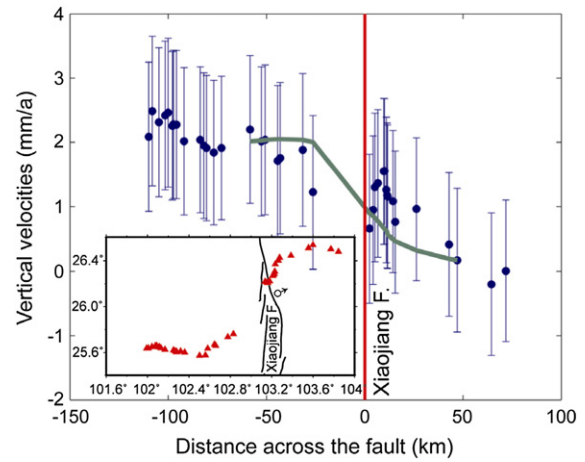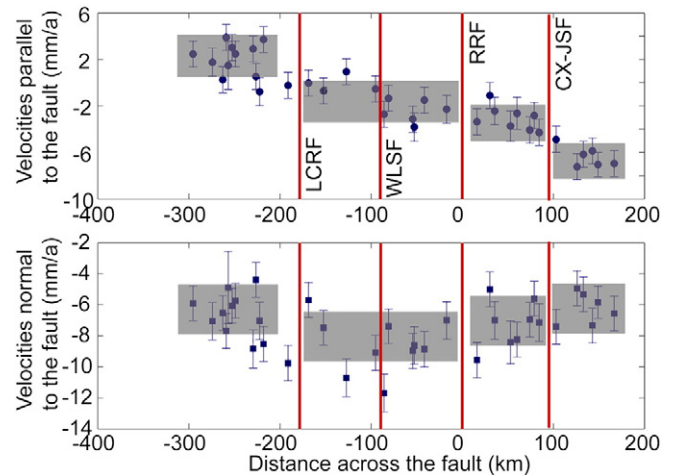


**Fig. 17.** GPS horizontal velocity profile across Red River fault. Data are from the rectangle (e) region in Fig. 1. Upper panel: Fault parallel component; bottom panel: fault-normal component. Abbreviations are: CXJSF, the Chuxiong–Jianshui fault; RRF, the Red River fault; WLSF, the Wuliang Shan fault; LCRF, the Lancang River fault.
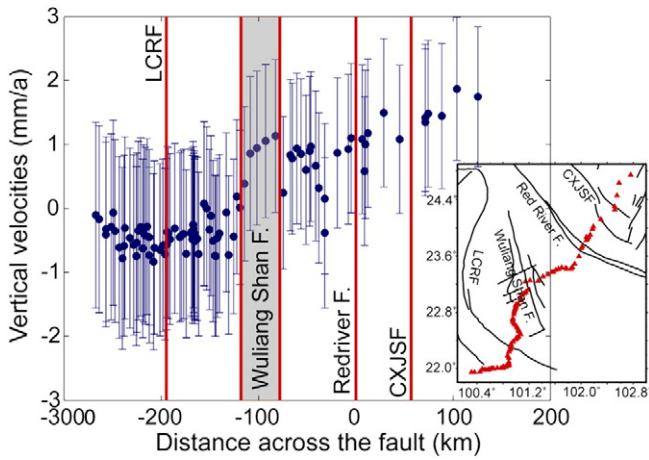
**Fig. 18.** Leveling vertical velocity profile across Red River fault. The velocities are plotted as a function of distance normal to the fault. The red triangles in the inset map are the locations of the leveling benchmarks. The gray shadow denotes the Wuliang Shan fault system. Abbreviations are: CXJSF, the Chuxiong–Jianshui fault; LCRF, the Lancang River fault.

Chuxiong–Jianshui and Lancang River faults located northeast and southwest of the Red River faults also show right-lateral motion with rates of 3.3 ± 0.7 and 0.9 ± 0.7 mm/a, respectively. The vertical velocity profile across the Chuxiong–Jianshui, Red River, and Lancang River faults indicates no significant vertical differential motion. However, across a 300 km range from the Lancang River fault to the Chuxiong–Jianshui fault (Fig. 18), there is a differential uplift motion of about 2 mm/a, with about 1 mm/yr differential motion across the Wuliang Shan fault system. No detectable horizontal deformation is observed in this fault system, suggesting perhaps partitioned horizontal and vertical motion across these sub-parallel fault systems. Thus the GPS and leveling results suggest that the Red River fault does not appear to be a dominant active fault in this region presently (Shen et al., 2005). The south boundary of the Sichuan–Yunnan block is therefore composed of several and distributed right lateral shear faults between the Chuxiong–Jianshui and Lancang River faults (M. Wang et al., 2003; Y.P. Wang et al., 2003; Zhang et al., 2003).

## 6. Discussion

### 6.1. The subsidence of central and southern Sichuan–Yunnan block

The vertical velocity field for the Sichuan–Yunnan block shows that the uplift rate of northern section is about 1–3 mm/a greater than the rate of central and southern sections in general. As a result, the central and southern sections are subsiding with respect to the northern section. The GPS profile normal to the Xiaojiang fault (Fig. 15) indicates that the southern Sichuan–Yunnan block exhibits ~4 mm/a east–west extension. Driven by the gravitational push, the southeast Tibetan Plateau is extruded eastward, and rotates clockwise along the Yushu–Xianshuihe fault around the Eastern Himalayan Syntaxis (EHS). The eastward subduction of the Indian plate underneath the Burma arc induces back-arc spreading in the upper plate, causing westward motion and east–west extension of the southern Sichuan–Yunnan block (Y.Z. Wang et al., 2008). Thus crustal motion and deformation pattern of the Sichuan–Yunnan block, including subsidence of its southern section with respect to the northern section, are manifested by both the gravitational collapse of the plateau and subduction of the India plate.

### 6.2. Horizontal material influx

It has been debated for the deformation mechanism of the Tibetan Plateau, and one school of thought advocates that the deformation is driven by the lower crustal flow (e.g. Flesch et al., 2001; Royden et al., 1997; Shen et al., 2001). If lower crustal flow exists, it should drive deformation in the entire crust, and its kinematics will be reflected somewhere at the Earth's surface and can be observed geodetically. However, to detect such movement of flow in the lower crust it is essential to acquire 3D deformation pattern at the surface. By combining horizontal GPS velocity field and leveling vertical displacement field this study provides such an opportunity.

To obtain a continuum horizontal velocity field we first interpolate the GPS derived horizontal station velocities using a method proposed by Shen et al. (1996). We then divide the eastern Tibetan Plateau into seven sub-blocks, and calculate the material influx rate of each sub-block using the horizontal velocity field derived in the last step. Assuming the net material influx of each sub-block results in crustal thickening and uplift, we compute the equivalent mean uplift rate as if the material influx is completely converted to vertical uplift, and compare that with the mean uplift rate estimated from the leveling data within that sub-block. The difference between the observed vertical uplift rate and that converted from the surface horizontal velocity field deduced material influx rate could be signal of lower crust flow.
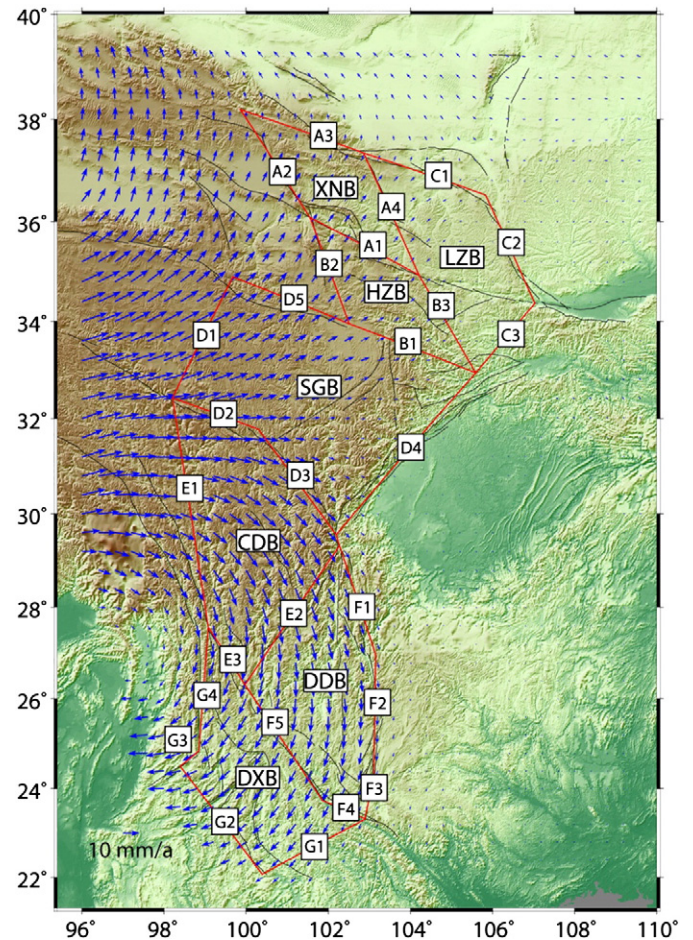


**Fig. 19.** Continuum distribution of horizontal velocity field with respect to south China interpolated from GPS horizontal velocity field. The red lines delineate the sub-block boundaries, and the letter codes on the sub-block boundaries denote the boundary segments. Crustal thickness data are from Ma et al. (1989). Abbreviations are: XNB, the Xining sub-block; LZB, the Lanzhou sub-block; HZB, the Hezuo sub-block; SGB, the Songpan–Ganzi sub-block; CDB, the Changdu sub-block; DDB, the Diandong sub-block; DXB, the Dianxi sub-block.

**Table 2**
Regional material net influx.

| Sub-block | Input (km³/a) $\Sigma_i L_i T_i V_i$ | Output (km³/a) $\Sigma_i L_i T_i V_i$ | Influx (km³/a) | Surface area ($\times 10^6$ km²) | $V_{GPS}$[a] (mm/a) | $V_{Leveling}$[b] (mm/a) |
|---|---|---|---|---|---|---|
| XNB | A1: $(135 \times 58 \times 5.7 + 70 \times 57 \times 4.6 + 65 \times 56 \times 3.4) \times 10^{-6} = 0.075$ <br> A2: $(70 \times 58 \times 3.8 + 64 \times 58 \times 4.8 + 63 \times 58 \times 5.6 + 77 \times 58 \times 5.6) \times 10^{-6} = 0.079$ | A3: $(64 \times 58 \times 4.3 + 48 \times 57 \times 4 + 72 \times 56 \times 4.2 + 93 \times 54 \times 3.6) \times 10^{-6} = 0.062$ <br> A4: $(82 \times 54 \times 4 + 57 \times 56 \times 4.5 + 47 \times 56 \times 4 + 46 \times 56 \times 3.7 + 64 \times 55 \times 3.2) \times 10^{-6} = 0.063$ | 0.029 | 0.048 | 0.6 | 1.7 ± 1.0 |
| HZB | B1: $(64 \times 58 \times 4 + 79 \times 54 \times 3.3 + 62 \times 50 \times 1.4 + 97 \times 46 \times 0.7) \times 10^{-6} = 0.036$ <br> B2: $(68 \times 58 \times 5.1 + 50 \times 59 \times 5.3 + 50 \times 60 \times 5.5 + 49 \times 59 \times 5.4 + 40 \times 59 \times 5.8) \times 10^{-6} = 0.082$ | A1: $(135 \times 58 \times 5.7 + 70 \times 57 \times 4.6 + 65 \times 56 \times 3.4) \times 10^{-6} = 0.075$ <br> B3: $(38 \times 54 \times 2.9 + 52 \times 50 \times 2.7 + 73 \times 48 \times 1.8 + 96 \times 46 \times 0.8) \times 10^{-6} = 0.023$ | 0.020 | 0.048 | 0.4 | 3.3 ± 1.1 |
| LZB | A4: $(82 \times 54 \times 4 + 57 \times 56 \times 4.5 + 47 \times 56 \times 4 + 46 \times 56 \times 3.7 + 64 \times 55 \times 3.2) \times 10^{-6} = 0.063$ <br> B3: $(38 \times 54 \times 2.9 + 52 \times 50 \times 2.7 + 73 \times 48 \times 1.8 + 96 \times 46 \times 0.8) \times 10^{-6} = 0.023$ | C1: $(55 \times 54 \times 3.6 + 38 \times 52 \times 3.2 + 71 \times 50 \times 2.5 + 44 \times 48 \times 1.9 + 77 \times 46 \times 1.4) \times 10^{-6} = 0.035$ <br> C2: $260 \times 44 \times 0.02 \times 10^{-6} = 0.0002$ <br> C3: $(70 \times 43 \times 0.3 + 146 \times 46 \times 0.4) \times 10^{-6} = 0.004$ | 0.047 | 0.083 | 0.6 | 3.8 ± 1.2 |
| SGB | D1: $(78 \times 69 \times 10.4 + 46 \times 67 \times 9 + 50 \times 66 \times 8.1 + 52 \times 65 \times 7.2 + 77 \times 64 \times 5.9) \times 10^{-6} = 0.164$ <br> D2: $(52 \times 69 \times 9 + 76 \times 67 \times 6.5 + 82 \times 65 \times 5.7) \times 10^{-6} = 0.096$ <br> D3: $(55 \times 64 \times 7 + 64 \times 62 \times 4.6 + 43 \times 60 \times 2.8 + 58 \times 54 \times 1.7 + 87 \times 52 \times 1) \times 10^{-6} = 0.060$ | D5: $(86 \times 63 \times 7.8 + 51 \times 62 \times 7.1 + 60 \times 61 \times 6.8 + 84 \times 60 \times 5.4) \times 10^{-6} = 0.117$ <br> B1: $(64 \times 58 \times 4 + 79 \times 54 \times 3.3 + 62 \times 50 \times 1.4 + 97 \times 46 \times 0.7) \times 10^{-6} = 0.036$ <br> D4: $(132 \times 45 \times 0.5 + 220 \times 44 \times 1.1 + 69 \times 46 \times 2.7 + 60 \times 50 \times 4.6) \times 10^{-6} = 0.036$ | 0.131 | 0.191 | 0.7 | 2.2 ± 1.2 |
| CDB | E1: $(72 \times 69 \times 17 + 49 \times 69 \times 17.7 + 46 \times 70 \times 16.7 + 45 \times 70 \times 14.2 + 46 \times 71 \times 12.2 + 46 \times 71 \times 10 + 44 \times 66 \times 8 + 39 \times 64 \times 6.6 + 50 \times 63 \times 4.9 + 57 \times 62 \times 3.2 + 58 \times 60 \times 1.6) \times 10^{-6} = 0.387$ | D2: $(52 \times 69 \times 9 + 76 \times 67 \times 6.5 + 82 \times 65 \times 5.7) \times 10^{-6} = 0.096$ <br> D3: $(55 \times 64 \times 7 + 64 \times 62 \times 4.6 + 43 \times 60 \times 2.8 + 58 \times 54 \times 1.7 + 87 \times 52 \times 1) \times 10^{-6} = 0.060$ <br> E2: $(67 \times 52 \times 7.8 + 94 \times 55 \times 8.7 + 68 \times 56 \times 8.7 + 76 \times 58 \times 6.9 + 100 \times 56 \times 5) \times 10^{-6} = 0.164$ <br> E3: $(71 \times 58 \times 5.5 + 94 \times 55 \times 7.6) \times 10^{-6} = 0.062$ | 0.005 | 0.139 | 0.04 | 1.7 ± 1.2 |
| DDB | E2: $(67 \times 52 \times 7.8 + 94 \times 55 \times 8.7 + 68 \times 56 \times 8.7 + 76 \times 58 \times 6.9 + 100 \times 56 \times 5) \times 10^{-6} = 0.164$ <br> F3: $(55 \times 50 \times 0.07 + 48 \times 46 \times 0.2 + 62 \times 42 \times 0.4 + 117 \times 38 \times 0.9) \times 10^{-6} = 0.006$ | F1: $(104 \times 50 \times 1.1 + 108 \times 52 \times 0.1 + 65 \times 54 \times 0.1) \times 10^{-6} = 0.007$ <br> F2: $(44 \times 53 \times 1.1 + 77 \times 52 \times 0.9) \times 10^{-6} = 0.006$ <br> F4: $117 \times 36 \times 6.1 \times 10^{-6} = 0.026$ <br> F5: $(124 \times 52 \times 8.3 + 70 \times 49 \times 8 + 85 \times 44 \times 7.9 + 62 \times 40 \times 8) \times 10^{-6} = 0.130$ | 0.001 | 0.120 | 0.01 | 1.3 ± 1.0 |
| DXB | E3: $(71 \times 58 \times 5.5 + 94 \times 55 \times 7.6) \times 10^{-6} = 0.062$ <br> F4: $117 \times 36 \times 6.1 \times 10^{-6} = 0.026$ <br> F5: $(124 \times 52 \times 8.3 + 70 \times 49 \times 8 + 85 \times 44 \times 7.9 + 62 \times 40 \times 8) \times 10^{-6} = 0.130$ | G1: $(164 \times 33 \times 2.3 + 130 \times 30 \times 2.1) \times 10^{-6} = 0.021$ <br> G2: $(100 \times 40 \times 8.8 + 76 \times 36 \times 8.8 + 80 \times 31 \times 7.2 + 82 \times 30 \times 6.2) \times 10^{-6} = 0.092$ <br> G3: $60 \times 44 \times 1.9 \times 10^{-6} = 0.005$ <br> G4: $(105 \times 54 \times 2 + 80 \times 52 \times 3.2 + 54 \times 48 \times 6.2 + 57 \times 48 \times 8) \times 10^{-6} = 0.063$ | 0.037 | 0.113 | 0.3 | 0.6 ± 1.4 |

[a] Average vertical velocity of each sub-block inferred from GPS horizontal crustal material influx.
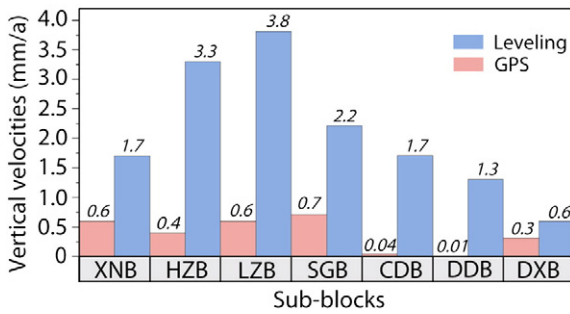[b] Average vertical velocity of each sub-block inferred from leveling data.

**Fig. 20.** Vertical rates of each sub-block inferred from horizontal material influx and leveling data.

The sub-blocks in Fig. 19 are constructed based on the GPS velocity result of Wang (2009) and the distribution of leveling benchmarks. The material influx for each sub-block is defined as

$$F = \sum_i L_i T_i V_i \tag{11}$$

where $L_i$ and $T_i$ are the length and crustal thickness of the $i$-th block boundary segment, and $V_i$ is the horizontal velocity perpendicular to that boundary segment. Each block boundary may have different crustal thickness and horizontal velocity, so the block boundary is divided into several parts. In the computation, we sum up the material influx over all the block segments for each sub-block, and the result is the net material injection or extrusion into or out of the sub-block.

As shown in Table 2 and Fig. 20, the uplift rates of the 7 sub-blocks in eastern Tibetan Plateau inferred from the horizontal crustal material influx are all less than that inferred from leveling measurements, respectively.

The horizontal material influx result shows that the movements of upper and lower crust seem to be quite different in most regions, namely, to maintain the uplift rate of each sub-block requires the influx rate of the lower crust and upper mantle higher than that of the upper crust, suggesting excessive lower crustal flow into the region. For example, the leveling determined uplift rates of the western, central, and eastern Songpan–Ganzi block (SGB) are 0–1 mm/a, 2–3 mm/a, and 0–1 mm/a, respectively. However, the average horizontal movement of the material in the lithosphere can only lead to an uplift rate of ~0.7 mm/a. This excessive vertical movement may reveal the existence of channel flow in the middle and lower crust under the Songpan–Ganzi block (SGB). During the process of eastward extrusion, the eastern part of the Tibetan Plateau is blocked by the stable Sichuan Basin, and the lower crustal materials possibly accumulated under the Longmen Shan range and western Sichuan plateau by viscous flow. Therefore, the middle and lower crust of the western Sichuan plateau is being thickened significantly, resulting in the uplift of the Longmen Shan range and western Sichuan plateau (Burchfiel et al., 2008; Zhang et al., 2009).

In the above estimation of vertical rates using horizontal data we did not account for the effect of isostatic readjustment during the crustal thickening process. This has to be the major error source for the estimate and its effect to our conclusion needs to be evaluated. When mass influx is positive the crust and lithosphere thicken, and isostatic adjustment drives part of the crust and lithosphere moving downward. To sustain vertical uplift rates derived from leveling data, more mass influx would have to occur through channel flow than our current estimate if isostatic adjustment is taken into account, therefore lending more support to our argument of mass influx through channel flow.

For other error sources, the one associated with taking the mean values of flux rates across the block boundaries has to be quite small since the flux rate variations are rather smooth. Some other error effects, however, are difficult to assess precisely, such as the ones associated with areal erosion rate and secular deformation rate at geological time scale. For that reason our conclusion is still preliminary and more works are needed in future study.

## 7. Conclusions

Based on the regional leveling observations collected in the eastern margin of the Tibetan Plateau, we obtain the present day crustal vertical velocity field, which can provide important quantitative numerical boundary constraints for regional tectonics, and help to understand the kinematic and geodynamic models. Combining the vertical velocity field acquired in this work and horizontal velocity field obtained by previous studies, we analyze the characteristics of the three-dimensional crustal movement of the eastern Tibetan Plateau. The primary conclusions are as follows.

(1) The trend of long-term crustal vertical movement obtained in this study is consistent with existing results inferred from geological methods, GPS, and leveling measurements. Most regions of the eastern margin of the Tibetan Plateau are in the status of uplift, especially the Gongga Shan uplifts at a maximum rate of $5.8 \pm 1.0$ mm/a, and the West Qinling is up at a maximum rate of $6.0 \pm 1.3$ mm/a.

(2) A 2-D buried faulting model is used to infer normal or reverse dip-slip rates. The result indicates that the reverse slip rate along the Longmen Shan fault is $4.2 \pm 0.5$ mm/a, followed by the Daliangshan and Longriba faults with the rates of $3.7 \pm 0.5$ mm/a and $2.8 \pm 0.3$ mm/a, respectively. The Zemuhe, and northern section of the Xiaojiang fault have the normal slip rates of $2.3 \pm 1.0$ mm/a and $2.9 \pm 0.4$ mm/a respectively.

(3) The regional three-dimensional velocity field indicates that the Helan Shan is uplifting and the Yinchuan graben is subsiding. The three-dimensional crustal movement of the Liupan Shan region is segmented, with the area in the vicinity of the northern Liupan Shan fault uplifting and the area in the vicinity of southern Liupan Shan fault subsiding respectively. The subsidence of the central and southern Sichuan–Yunnan block relative to the northern part is caused by the near east–west extension. The south boundary of Sichuan–Yunnan block is composed of several distributed right lateral shear faults between the Chuxiong–Jianshui and Lancang River faults.

(4) The comparison of vertical velocities inferred from the crustal material influx and from leveling data in the eastern margin of the Tibetan Plateau lends support to a model with the channel flow in the lower crust.

## References

Burchfiel, B.C., Royden, L.H., van der Hilst, R.D., Hager, B.H., 2008. A geological and geophysical context for the Wenchuan earthquake of 12 May 2008, Sichuan, People's Republic of China. GSA Today 18 (7), 4–11.

Chai, Z.Z., Meng, G.K., Ma, G.R., 2011. Active Faults Exploration and Seismic Hazard Assessment of Yinchuan City. Science Press, pp. 45–46 (in Chinese).

Chen, Z., Burchfiel, B.C., Lin, Y., King, R.W., Royden, L.H., Tang, W., Wang, E., Zhao, J., Zhang, X., 2000. Global positioning system measurements from Eastern Tibet and their implications for India/Eurasia intercontinental deformation. J. Geophys. Res. 105 (B7), 16215–16227.

Clark, M.K., Royden, L.H., 2000. Topographic ooze: building the eastern margin of Tibet by lower crustal flow. Geology 28 (8), 703–706.

D'Anastasio, E., De Martini, P.M., Selvaggi, G., Pantosti, D., Marchioni, A., Maseroli, R., 2006. Short-term vertical velocity field in the Apennines (Italy) revealed by geodetic leveling data. Tectonophysics 418, 219–234.

Deng, Q., Zhang, P., Ran, Y., Yang, X., Min, W., Chu, Q., 2003. Basics characteristics of active tectonics of China. Sci. China 46 (4), 356–372.

Ding, G.Y. (Ed.), 1991. Lithospheric Dynamics of China. Seismological Press, Beijing, p. 600 (in Chinese).

Duong, C., Feigl, K.L., 1999. Geodetic measurement of horizontal strain across the Red River fault near Thac Ba, Vietnam, 1963–1994. J. Geod. 73, 298–310.

England, P., McKenzie, D., 1982. A thin viscous sheet model for continental deformation. Geophys. J. Int. 70, 295–321.

England, P.C., Molnar, P., 1997. Active deformation of Asia: from kinematics to dynamics. Science 278, 647–650.

Feigl, K.L., Duong, C., Becker, M., To, Tran Din, Neumann, K., Xuyen, Nguyen Quang, 2003. Insignificant horizontal strain across the Red River fault near Thac Ba, Vietnam from GPS measurements 1994–2000. Geophys. Res. Abstr. 5 (Abstract 04707).

Flesch, L.M., Holt, W.E., Haines, A.J., 2001. Dynamics of the India–Eurasia collision zone. J. Geophys. Res. 106, 16435–16460.

Present-day vertical motion of the Tibetan Plateau and surrounding area. In: Freymueller, J.T., Fu, Y., Wang, Q., Xu, C.J., Leech, M.L., et al. (Eds.), Proceedings for the 25th Himalaya–Karakoram–Tibet Workshop (1 pp.).

Gan, W., Zhang, P., Shen, Z.-K., Niu, Z.J., Wang, M., Wan, Y.G., Zhou, D.M., Cheng, J., 2007. Present-day crustal motion within the Tibetan Plateau inferred from GPS measurements. J. Geophys. Res. 112, B08416.

Guo, S.M., Ji, F.J., Xiang, H.F., 2001. The Honghe Active Fault Zone. Oceanology Press, Beijing, pp. 86–108 (in Chinese).

Han, W.B., Jiang, G.F., 2005. Study on seismicity of daliangshan and Anninghe–Zemuhe fault zones. J. Seismol. Res. 28 (3), 207–212 (in Chinese).

Houseman, G., England, P., 1986. Finite strain calculations of continental deformation 1: method and general results for convergent zones. J. Geophys. Res. 91, 3651–3663.

Hubbard, Judith, Shaw, John H., 2009. Uplift of the Longmen Shan and Tibetan plateau, and the 2008 Wenchuan (M = 7.9) earthquake. Nature 458, 194–197.

Jackson, D.D., Matsu'ura, M., 1985. A Bayesian approach to nonlinear inversion. J. Geophys. Res. 90, 581–591.

Kirby, E., Reiners, P., Krol, M., Whipple, K.X., Hodges, K.V., Farley, K.A., Tang, W., Chen, Z., 2002. Late Cenozoic uplift and landscape evolution along the eastern margin of the Tibetan Plateau: inferences from $^{40}Ar/^{39}Ar$ and (U–Th)/He thermochronology. Tectonics 21 (1), 1001.

Kirby, E., Whipple, K.X., Tang, W., Chen, Z., 2003. Distribution of active rock uplift along the eastern margin of the Tibetan Plateau: inferences from bedrock channel longitudinal profiles. J. Geophys. Res. 108 (B4), 2217.

Lai, X.A., Huang, L.R., Xu, J.S., 2004. Present-Day Crustal Movement in China Constrained. Seismological Press, Beijing (in Chinese).

Lease, R.O., Burbank, D.W., Clark, M.K., Farely, K.A., Zheng, D., Zhang, H., 2011. Middle Miocene reorganization of deformation along the northeastern Tibetan Plateau. Geology 39 (4), 359–362.

Liang, S., Gan, W., Shen, C., Xiao, G., Liu, J., Chen, W., Ding, X., Zhou, D., 2013. Three-dimensional velocity field of present-day crustal motion of the Tibetan Plateau derived from GPS measurements. J. Geophys. Res. Solid Earth 118.

Ma, X.Y., Ding, G.Y., Zhang, H.G., Zhang, B.C., Ma, Z.J., 1989. Lithospheric Dynamics Atlas of China. China Cartographic Publishing House, pp. 1–68 (in Chinese).

Ma, Q., Huang, L.R., Ma, Z.J., Zhang, J., 2003. Recent crustal vertical movement in the so-called central axis structure zone in the continent of China. Acta Geol. Sin. 77 (1), 35–43 (in Chinese).

Niu, Z.J., Ma, Z.J., Chen, X.L., Zhang, Z.S., Wang, Q., You, X.Z., Sun, J.Z., 2002. Crustal movement observation network of China. J. Geodesy Geophys. 22 (3), 1–7 (in Chinese).

Okada, 1985. Surface deformation due to shear tensile faults in a half space. Bull. Seismol. Soc. Am. 75 (4), 1135–1154.

Peltzer, G., Tapponnier, P., 1988. Formation and evolution of strike-slip faults, rifts, and basins during the India–Asia collision — an experimental approach. J. Geophys. Res. 93 (B12), 15085–15117.

Replumaz, A., Tapponnier, P., 2003. Reconstruction of the deformed collision zone between India and Asia by backward motion of lithospheric blocks. J. Geophys. Res. 108 (B6), 2285.

Royden, L.H., Burchfiel, B.C., King, R.W., Wang, E., Chen, Z., Shen, F., Liu, Y., 1997. Surface deformation and lower crustal flow in eastern Tibet. Science 276, 788–790.

Shen, Z.-K., Jackson, D.D., Ge, B.X., 1996. Crustal deformation across and beyond the Los Angeles basin from geodetic measurements. J. Geophys. Res. 101, 27957–27980.

Shen, F., Royden, L.H., Burchfiel, B.C., 2001. Large-scale crustal deformation of the Tibetan Plateau. J. Geophys. Res. 106, 6793–6816.

Shen, Z.-K., Lü, J., Wang, M., Bürgmann, R., 2005. Contemporary crustal deformation around the southeast borderland of the Tibetan Plateau. J. Geophys. Res. 110, B11409.

Shen, Z.K., Sun, J.B., Zhang, P.Z., Wan, Y., Wang, M., Bürgmann, R., Zeng, Y., Gan, W., Liao, H., Wang, Q., 2009. Slip maxima at fault junctions and rupturing of barriers during the 2008 Wenchuan earthquake. Nat. Geosci. 2, 718–724.

Standardization Administration of the People's Republic of China, 2006. Specifications for the First and Second Order Leveling. National Standard of the People's Republic of China, GB/T (12897–2006, in Chinese).

Tan, X.B., Xu, X.W., Lee, Y.H., Chen, G.H., Wan, J.L., 2010. Apatite fission track evidence for rapid uplift of the Gongga Mountain and discussion of its mechanism. Chin. J. Geophys. 53 (8), 1859–1867 (in Chinese).

Tapponnier, P., Peltzer, G., Le Dain, A.Y., Armijo, R., Cobbold, P., 1982. Propagating extrusion tectonics in Asia: new insights from simple experiments with plasticine. Geology 10 (12), 611–616.

Wan, Y.G., Shen, Z.K., Wang, M., Zhang, Z.S., Gan, W.J., Wang, Q.L., Sheng, S.Z., 2008. Coseismic slip distribution of the 2001 Kunlun mountain pass west earthquake constrained using GPS and InSAR data. Chin. J. Geophys. 51 (4), 753–764.

Wang, M., 2009. Analysis of GPS Data With High Precision and Study on Present-Day Crustal Deformation in China(Doctoral thesis) Institute of Geology, China Earthquake Administration (in Chinese).

Wang, Q., Zhang, P.Z., Freymueller, J.T., Bilham, R., Larson, K.M., Lai, X., You, X., Niu, Z., Wu, J., Li, Y., Liu, J., Yang, Z., Chen, Q., 2001. Present-day crustal deformation in China constrained by Global Positioning System measurements. Science 574–577.

Wang, M., Shen, Z.K., Niu, Z.J., Zhang, Z.S., Sun, H.R., Gan, W.J., Wang, Q., Ren, Q., 2003a. Present crustal movement and active block model of continental China. Sci. China Ser. D Earth Sci. 33, 21–32 (Suppl., in Chinese).

Wang, Y.P., Shen, J., Wang, Q., 2003b. On the lateral extrusion of Sichuan–Yunnan block. Earth Sci. Front. 10, 188–192 (Suppl., in Chinese).

Wang, Y.Z., Wang, E.N., Shen, Z.K., Wang, M., Gan, W.J., Qiao, X.J., Meng, G.J., Li, T.M., Tao, W., Yang, Y.L., Cheng, J., Li, P., 2008a. GPS-constrained inversion of present-day slip rats along major faults of the Sichuan–Yunnan region. Sci. China Ser. D Earth Sci. 51 (9), 1267–1283.

Wang, Q.L., Cui, D.X., Wang, W.P., Zhang, S.X., Liu, J.W., Shi, Q., 2008b. Present vertical crustal displacements of western Sichuan region. Sci. China Ser. D Earth Sci. 38 (5), 598–610 (in Chinese).

Weldon, R., Sieh, K., Zhu, O., Han, Y., Yang, J., Robinson, S., 1994. Slip rate and recurrence interval of earthquakes on the Hong He (RedRiver) fault, Yunnan, PRC. Paper Presented at International Workshop Seismotectonics and Seismic Hazard in South East Asia. UNESCO, Hanoi.

Wessel, P., Smith, W., 1991. Free software helps map and display data. EOS Trans. Am. Geophys. Union 72 (441), 445–446.

Xu, X.W., Wen, X.Z., Chen, G.H., Yu, G.H., 2008. Discovery of the Longriba fault zone in eastern Bayan Har block, China and its tectonic implication. Sci. China Ser. D Earth Sci. 51 (9), 1209–1223.

Zhang, P.Z., Wang, M., Gan, W.J., 2003. Slip rates along major active faults from GPS measurements and constrained on contemporary continental tectonics. Earth Sci. Front. 10, 81–92 (Suppl. in Chinese).

Zhang, P.Z., Shen, Z.K., Wang, M., Gan, W.J., Bürgmann, R., Molnar, P., Wang, Q., Niu, Z., Sun, J., Wu, J., Sun, H., You, X., 2004. Continuous deformation of the Tibetan Plateau from Global Positioning System data. Geology 32 (9), 809–812.

Zhang, P.Z., Wen, X.Z., Xu, X.W., Gan, W.J., Wang, M., Shen, Z.K., 2009. Tectonic model of the great Wenchuan earthquake of May 12, 2008, Sichuan, China. Chin. Sci. Bull. 54 (7), 944–953 (in Chinese).